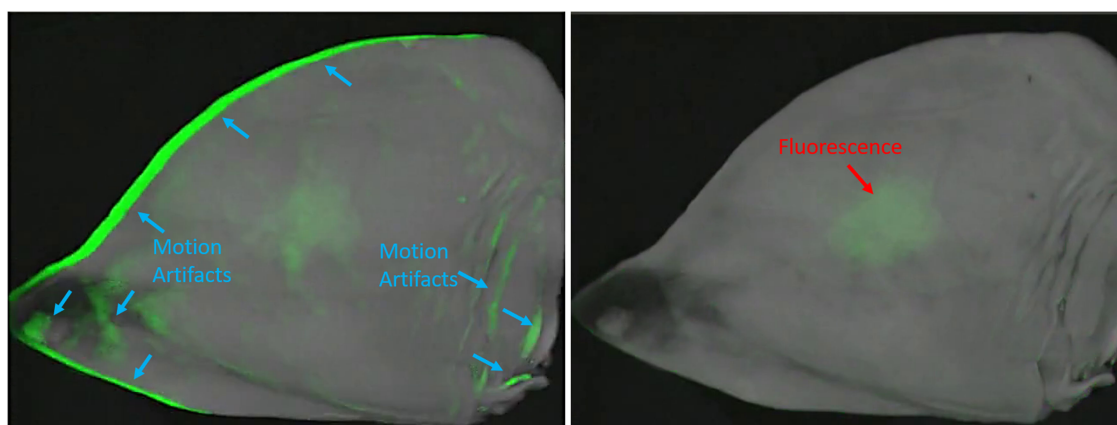


Enhance Fluorescence Imaging and Remove Motion Artifacts by Combining Pixel Tracking, Interleaved Acquisition, and Temporal Gating


Volume 13, Number 1, February 2021

Christopher Mela
Francis Papay
Yang Liu, *Member, IEEE*



DOI: 10.1109/JPHOT.2021.3055809

Enhance Fluorescence Imaging and Remove Motion Artifacts by Combining Pixel Tracking, Interleaved Acquisition, and Temporal Gating

Christopher Mela,^{2,3} Francis Papay,⁷
and Yang Liu ^{1,3,4,5,6} *Member, IEEE*

¹Department of Electrical and Computer Engineering, The University of Iowa, IA City, IA 52242 USA

²Department of Biomedical Engineering, The University of Akron, Akron, OH 44325 USA

³University of Iowa Technology Institute, The University of Iowa, IA City, IA 52242 USA

⁴Iowa Institute for Biomedical Imaging, The University of Iowa, IA City, IA 52242 USA

⁵Center for Bioinformatics and Computational Biology, The University of Iowa, IA City, IA 52242 USA

⁶Iowa Informatics Initiative, The University of Iowa, IA City, IA 522424 USA

⁷Dermatology & Plastic Surgery Institute, Cleveland Clinic, Cleveland, OH 44195 USA

DOI:10.1109/JPHOT.2021.3055809

This work is licensed under a Creative Commons Attribution-NonCommercial-NoDerivatives 4.0 License. For more information, see <https://creativecommons.org/licenses/by-nc-nd/4.0/>

Manuscript received November 29, 2020; revised January 22, 2021; accepted January 23, 2021. Date of publication February 1, 2021; date of current version February 15, 2021. This work was supported in part by the University of Iowa Startup Funds and National Aeronautics and Space Administration (NASA) (NNX14AL37H) and in part by the U.S. Air Force under Agreement FA8650-16-2-6702 and Frederick Gardner Cottrell Foundation Grant. Corresponding author: Yang Liu (e-mail: yang-liu-ec@uiowa.edu).

This article has supplementary downloadable material available at <https://doi.org/10.1109/JPHOT.2021.3055809>, provided by the authors.

Abstract: Fluorescence imaging has been applied to improving many medical sub-specialties. In a clinical setting, there are motions of the imaging system and patients, as well as a high ambient light background. This presents a challenge for widely using fluorescence imaging systems clinically. In this paper, we present a novel approach combining computer vision and pulsed imaging system for enhanced fluorescence Imaging and motion artifacts removal. Specifically, we use a dense optical flow point tracking regime in conjunction with pulsed fluorescence excitation and interleaved acquisition. The system was characterized with respect to fluorescent detection sensitivity, using a clinically relevant fluorescent environment, and the results were compared to conventional steady-state (DC) fluorescence imaging. We also characterized the system with respect to fluorescence detection accuracy. We demonstrated a 45-fold reduction of motion artifacts by combining pixel tracking and fluorescence pixel identification with pulsed light imaging. Furthermore, the fluorescence imaging signal-to-background ratio is also improved for more than 2-fold. Our results indicate that pixel tracking, temporal gating, and interleaved acquisition can improve fluorescence imaging, especially for uses in realistic clinical settings where there is a high ambient light background.

Index Terms: Biophotonics, medical photonics, fluorescence imaging, computer vision, optical imaging, image-guided surgery, real-time imaging, cyber-physical systems.

1. Introduction

Image-guided surgery and intervention aided by fluorescence have been applied to many medical sub-specialties, including surgical oncology, plastic surgery, lymphatic surgery, neurosurgery, cardiothoracic surgery, dermatology, minimally invasive surgery, robotic surgery, microsurgery, etc. Fluorescence imaging can identify blood vessels, lymph nodes, and cancerous lesions intraoperatively [1]–[3]. Significant attention has been directed to intraoperative fluorescence imaging in recent years [4]–[12]. Many methods have been used to improve fluorescence detection for intraoperative imaging. The most basic of these include the use of software-based thresholding and hardware-based optical filters to separate the fluorescent emissions from background reflectance [13]–[17]. The drawback of using these methods alone is a significant reduction in the ability to accurately localize the fluorescent source on the anatomical landscape. Remedies to this pitfall have come in the form of co-registration of the fluorescent information to the background, or anatomical, data which is simultaneously captured on a separate unfiltered imaging sensor. Such techniques have been implemented through various means, including beam splitter hardware [18]–[21] and software based registration [16], [22], [23]. A simpler, though less discrete method, involves using a broader imaging filter that allows some near-infrared emission wavelength light into the excitation light source [24]. While these methods help resolve the localization issue, they are often insufficient to improve detection sensitivity in a realistic environment.

In a realistic setting such as the operating room, both room and surgical lights are used and contribute to background reflectance in the fluorescence images, reducing the signal-to-background ratio and image contrast. Pulsed light imaging has emerged as a simple and efficient way to improve fluorescence detection, regardless of hardware regime, separating the signal from the background based on the temporal frequency of fluorescent emissions [25]–[30]. Techniques for pulsed light imaging involve synchronizing camera captures with excitation ON and OFF states incurred during excitation light pulsation [29], [31], [32]. In this way, sequential images can be obtained both with and without fluorescence emissions. The images taken during the OFF state of the excitation light source, without fluorescence, serve as reference background reflectance frames to be subtracted from the ON state images, effectively removing any non-fluorescence light detected. Other techniques include applying phase modulation to recreate a pulsed style excitation [29], as well as synchronization of the camera captures with the frequency of the room lights rather than the excitation light [27], [28]. Pulsed light is often used in conjunction with other fluorescence imaging enhancement tools. In particular, the method has been implemented for co-registration of fluorescence with color reflection mode imagery [29], [31], [32].

A potential issue arising when subtracting fluorescent and background frames for pulsed light imaging is motion artifacts. Imaging systems using pulsed light are typically either stand-mounted or handheld and used in contact mode. While target or camera motion may not be an issue in benchtop studies, such motions are very typical in clinical settings. Intraoperatively, a fluorescent target may move, or an object may pass in front of the target (e.g., hand, surgical instruments). For a wearable intraoperative imaging system, such as the system described herein, the cameras are head-mounted and subject to movements. Even when using relatively high framerates (60-120 fps), head movements and hand motions conducted within the surgical imaging field can result in motion artifacts. This is because the positions of objects in motion are no longer at the same location in sequentially subtracted frames. The inter-frame correspondence between pixels in subsequent frames changes due to motion, leading to artifacts when subtracting interleaved frames. Increasing the framerate can decrease inter-image object disparity but will not remove it completely.

In this paper, we present a novel approach combining computer vision with a pulsed light imaging system for enhanced fluorescence imaging and motion artifact removal. Specifically, we use a dense optical flow point tracking regime in conjunction with pulsed fluorescence excitation and interleaved acquisition. The system was characterized with respect to fluorescence detection sensitivity, using a clinically relevant fluorescent environment, and the results were compared to conventional steady-state (DC) fluorescence imaging. We also characterized the system with respect to fluorescence detection accuracy.

2. Materials and Methods

2.1 Computation

Camera control, image processing, output to display, and coordination of light pulsation were integrated on a mini PC (NUC6i7KYK Intel WA, USA). Computer specifications were as follows: 32GB 2133 MHz DDR4 Ram, 500 GB SSD, Intel Core i7-6770HQ processor at 2.6 GHz per core with Intel Iris Pro 580 integrated graphic card. Achieving higher frame rates while reducing registration latency was accomplished by GPU computing using the integrated Intel Iris Pro 580 graphics card. The system was operated using Ubuntu 16.04 LTE. A software program was designed for camera control and capture, pulsed light integration, point tracking, fluorescence segmentation and display output. All software was written using Python and associated programming libraries, including the Open source Computer Vision (OpenCV) libraries. The point tracking and fluorescence segmentation algorithms, located within the main loop, were sent to the GPU for processing using the Just-In-Time (JIT) package within the Numba libraries (Anaconda, TX, USA). A separate microcontroller (Atmel ATmega328p) was used to modulate the excitation light source pulsation. The module communicated with the mini PC via USB port, allowing image capture/pulsed excitation synchronization.

2.2 Instrumentation

The fluorescence imaging system used here integrated two high-speed CCD sensors (MC023MG-SY Ximea, DEU) with high-efficiency, low distortion machine vision lenses (M118FM08 Tamron, JPN) and narrow band filters (65-166 Edmund Optics, NJ, USA). Filters, centered at 632 nm, were applied to minimize out of band noise. The sensors were operated at a full-resolution of 2.3 megapixels. The frame rate, however, was not set, since the cameras captured images upon receiving a trigger signal from the computer, synchronized with the excitation pulses. The cameras were connected to the computer via USB 3.1 connections. Additional camera parameters included a 10 dB gain and 10 ms exposure time. A 405 nm LED emitter with adjustable collimation (M405L3 & SM2F32-A ThorLabs, NJ, USA) was used for fluorescence excitation. The excitation bandwidth was limited between 400–450 nm using a bandpass filter (84-781 Edmund Optics, NJ, USA). Additionally, broadband light for reflectance mode background/anatomical imaging was provided using a white LED emitter, collimated and focused through an adjustable aspheric lens with 400–700 nm anti-reflection filter (MNWHL4 & SM2F32-A ThorLabs, NJ, USA). To prevent contamination of fluorescent emissions with similar reflected wavelengths from the white light source, a 632 ± 5 nm bandstop filter was applied to the LED. Both LEDs were operated using adjustable output driver circuits (LEDD1B ThorLabs, NJ, USA).

2.3 Light Pulsation and Interleaved Acquisition

Light pulsation was triggered using a microcontroller (Atmel ATmega328p) and its GPIO ports, implemented on a microcontroller development board (Arduino Uno, ITA). The circuit was programmed to output a square waveform with a 50% duty cycle, a pulse width of 20 ms and an amplitude of 1 or 0. Connections between the microcontroller board, the LED excitation light source and the computer followed the diagram below, Fig. 1(a), and the pulse cycle is represented in Fig. 1(b). When the output pulse train from the microcontroller reached a high state (value = 1), the excitation light was switched on. During the waveform's low pulse state (value = 0), the light remained off. The microcontroller was also connected to the PC via USB for power and data communication. Whenever a pulse state was read in by the PC, a camera capture was triggered after a brief (20 μ s) delay allowing the LED to reach a full ON or OFF state. The returned image was then classified as high or low, depending on whether the returned state was 1 or 0, respectively.

Sequential high and low state images were subtracted to return a difference image. Pixels containing fluorescence information appeared bright in the resultant subtraction. Limited speckle-noise also appeared due to frame-to-frame variation in pixel values, and was treated with an erosion

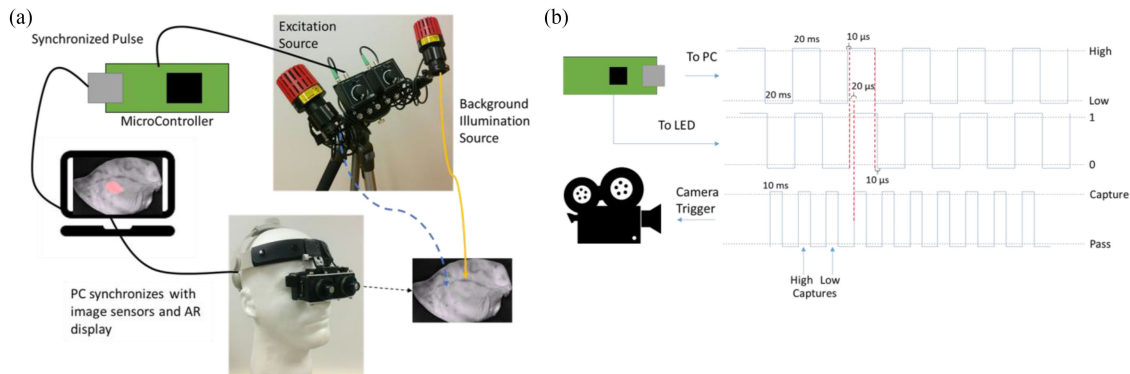


Fig. 1. System setup and timing diagram. (a) System including wearable stereoscopic fluorescence imaging with augmented reality near-eye display, light source offering both fluorescence excitation and background reflectance, a microcontroller, and a mini PC. (b) Timing diagram for light pulsation and interleaved acquisition. Signal pulse trains from the microcontroller to the PC and the excitation LED, and the trigger signal from the PC to the camera are shown. The pulses from the microcontroller to the PC and LED were of the same width, but the LED waveform was delayed by $10\ \mu\text{s}$ from the PC bound waveform to allow for processing time. Camera captures occurred after each high and low pulse was received from the microcontroller following a $20\ \mu\text{s}$ delay to account for LED rise and fall times, to avoid frame capture during a transient state. Camera exposure was set to one half the pulse width for the same reason.

filter. Any additional background still present was treated with a low-threshold binary filter on the difference image, and the binary output of this operation was used for point tracking. Prior to display, the binary output was subjected to a mean blur filter with a 5×5 kernel to smooth small gaps or errors in the fluorescence region. The algorithm is described graphically in the flowchart below, Fig. 2.

Tests were conducted to verify the timing and to count the number of missed states. A missed state is here defined as a misidentified capture taken by the camera, i.e., a high state identified capture taken during a low or transient LED pulse state, or a capture identified as low state taken during a high or transient LED state. The LED pulse state was confirmed using an independent light meter operated in temporal alignment with the imaging system. At each camera capture, the intensity of the LED pulse was read. A high pulse corresponded to a light meter reading of at least $1\ \text{mW}/\text{cm}^2$, and a low pulse corresponded to readings of $0.1\ \text{mW}/\text{cm}^2$, and a transient state corresponded to any readings lower than $0.95\ \text{mW}/\text{cm}^2$ and greater than $0.15\ \text{mW}/\text{cm}^2$, affording a 5% error in either direction. The number of missed states was determined over a 2 minute period, beginning after the system reached steady-state operation. Two different operating modes were tested in this way: a no motion test in which the camera was mounted and a high motion test during which the camera was translated in the x and y planes on a moving stage in an asterisk pattern (*). The motion tests were conducted at $0.05\ \text{m}/\text{s}$ translation speed, and each test was averaged over 5 trials.

2.4 Fluorescent Point Tracking

In order to properly track which points were pulsing in sync with the excitation light source, all points in the frame, or at least all points within a select region, must be tracked. A sparse flow optical tracking algorithm, such as the Lucas Kanade method [33], [34], proved to be an invalid option in this case, as it did not track all fluorescent pixels. Therefore, we implemented the Farneback dense flow optical tracking method to track the pixel flow between imaging frames [34], [35]. The pixel motion between the previous and current imaging frames, described as positive or negative changes in the x and y coordinate plane, designated Δx and Δy , was used to determine each pixel's position in the current frame. All pixel positions were known during the first frame of camera capture, corresponding to their original x-y coordinates. In each of the following sequential frames,

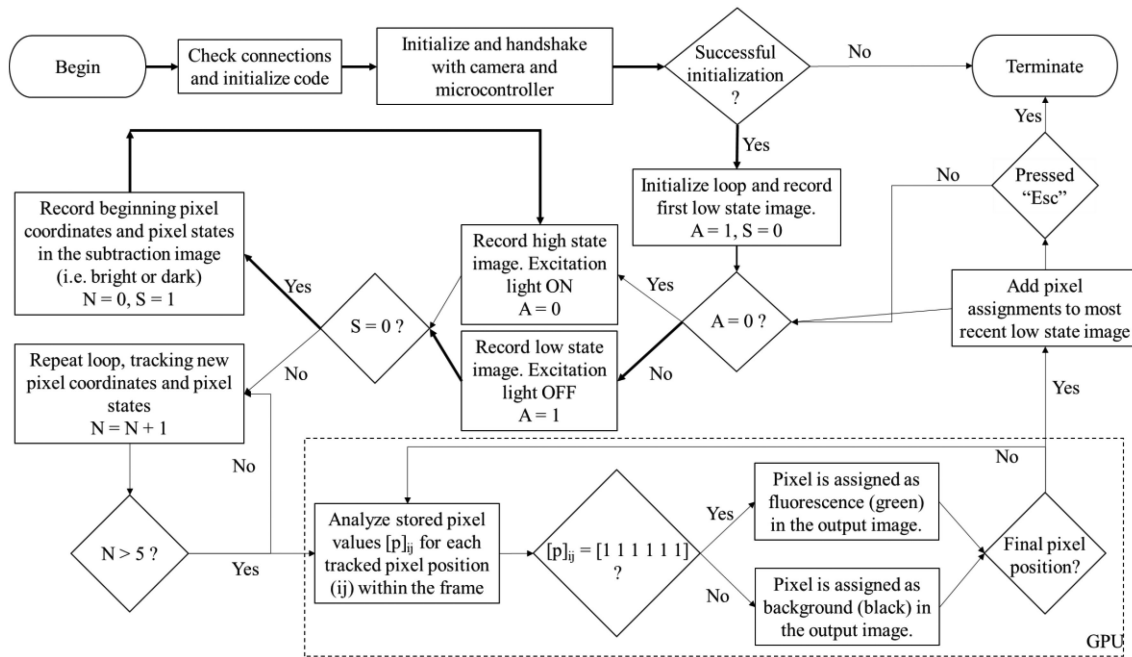


Fig. 2. Flowchart depicting the algorithms for interleaved imaging frame capture, pixel tracking, and fluorescence classification. The segment enclosed in the dashed box at the lower right was sent to the onboard GPU for parallel processing to speed up fluorescence classification of pixels. Bold arrows indicate the system initialization path.

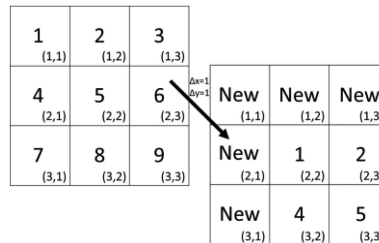


Fig. 3. Illustration of pixel motion between sequential image frames. In this example, the movement of pixel 1 from the (i,j)th coordinate point (1,1) to the point (2,2). Per (1) & (2), this results in a Δx and Δy of 1. As the pixels shift diagonally to the lower right, new pixels enter the screen from the top left. These new pixels will be tracked beginning with the next frame in the series.

each pixel’s coordinate changed according to (1) and (2), where c was the current pixel coordinate and p was the previous coordinate in either the x or y axis. An example of pixel motion is illustrated in Fig. 3.

$$x_c = x_p + \Delta x_{c-p} \tag{1}$$

$$y_c = y + \Delta y_{c-p} \tag{2}$$

The current position of each pixel in the aforementioned binary output (Section 2.3) was monitored, and its corresponding binary value (1 or 0, dependent on the presence or absence of fluorescence, respectively) was recorded. Frames were captured, and both coordinates and binary values were recorded for each pixel over several loop cycles (N). The number of loops in each cycle was varied for optimization. Fluorescence identification and segmentation began after $N + 1$

loops had elapsed. During each cycle, pixels which alternated between high and low states in the same sequence as the pulsed excitation signal from the microcontroller were determined to be fluorescent. The locations of the fluorescent pixels in the current frame were overlain onto the next low state image using a pseudocolor to highlight the fluorescence areas for viewing.

2.5 Fluorescence Imaging Sensitivity

Fluorescence imaging sensitivity measurements were conducted in both pulsatile and non-pulsatile mode on stationary targets, with the system cameras fixed at a 40 cm working distance. The purpose of these fluorescence tests was to compare the sensitivity of the system in both modes of operation, to determine whether our pulsed imaging regime improves fluorescence detection. Tests were conducted using 2 mL tissue phantoms prepared, as described by Wagnieres [36], using intralipid, silica and India ink as the scattering and absorbing agents, respectively. Varying concentrations of Protoporphyrin IX (PpIX) were dissolved in DMSO and added to the phantoms, in the following concentrations: 0, 3, 6.25, 12.5, 25, 50, 100, 200 and 300 nM. Phantoms were dispensed into 24-Well plates (Eppendorf, DEU) for analysis, alternating fluorescent and non-fluorescent phantoms to prevent cross contamination of emissions. Fluorescent emissions were induced using excitation intensities of 4000, 2000, 1000, 500 and 250 $\mu\text{W}/\text{cm}^2$. The required dye concentrations to achieve a range of signal-to-background ratios (SBRs) were calculated for each excitation intensity. Minimum successful fluorescence detection was determined at an SBR of 2. Tests were repeated over $n = 5$ trials, and multiple factor ANOVA was used to compare pulsed and non-pulsed results for significant differences (CI = 95%, $\alpha = 0.05$). Additionally, post-hoc analyses were conducted using a Tukey test to elucidate pulsed versus steady-state grouping.

Evaluation of fluorescence sensitivity limits on porcine skin was conducted. Solutions of PpIX in DMSO, at varying dye concentrations, were applied topically to the pig skin in 50 μL volumes via cotton swab. Due to the high level of naturally occurring porphyrins in skin tissue, we tested higher concentrations for this application than for raw fluorescent detection tests using the well plates, due to the higher autofluorescent background: 30, 60, 100, 200, 300, 500, 1000, 2000 and 4000 nM. Imaging was conducted using both pulsatile and non-pulsatile modes at the same excitation levels reported above, and the results were compared for difference via ANOVA and Tukey test ($n = 5$, CI = 95%, $\alpha = 0.05$).

2.6 Evaluation of Fluorescent Point Tracking Accuracy

The accuracy of the pulsed regime in detecting real fluorescence pixels, versus noise or motion artifacts, was tested. Additionally, the system was tested on missed fluorescence pixel detection. A cell culture dish (Eppendorf, DEU) was filled with a 300 nM PpIX/DMSO solution. The plate was placed on top of a tissue phantom block, which was placed on a black, non-reflective surface. The cameras were mounted parallel to, and directly overhead of the plate at a 40 cm working distance. The PpIX solution was illuminated using the pulsed excitation light source. Illumination intensity was set to a level that allowed all visible fluorescence to be uniformly detected at pixel values between 175 and 200 on the gray scale (0-255). In this way, we prevented sensor saturation, and allowed bright pixels to be easily counted within each image. A binary threshold was applied to the image and a simple edge detector was used to determine the outer border of the imaged plate. The number of white pixels (i.e., identified as fluorescent) within and without the plate borders were averaged over multiple frames ($n = 55$) to serve as a baseline. Pulsatile imaging was then initiated, using the described method. The number of fluorescent pixels detected within and without the circle of the cell culture plate were counted at multiple random time points ($n = 11$) as the cameras were translated in an asterisk pattern above the plate to simulate user motion. During and following each movement, counts were taken of the number of fluorescently labeled pixels within the area of the plate. Additional counts were taken within the tissue phantom area, but outside of the plate, as well as on the dark desktop background in each image. Counts were taken using the binary subtraction image data overlaid onto the low-state image for localization. The counts were then divided by the

total number of pixels in each image region (plate, phantom, or desktop). Counts were converted to a percentage, with the target optimal values being 100% fluorescence within the culture plate and 0% fluorescence on the phantom and desktop. The entire motion test was repeated over 5 trials, resulting in $n = 55$ frames. Fluorescent pixel identification accuracy was calculated using the (3-7) for each of the image regions: fluorescent tissue, non-fluorescent tissue, and background. Accuracy was assessed in both high and low pulse states, on a per pixel basis.

$$|P_{ij} - I_{ij}| > 0 \rightarrow E_{ij}^m = 1 \quad (3)$$

$$|P_{ij} - I_{ij}| = 0 \rightarrow E_{ij}^m = 0 \quad (4)$$

$$Total_Errors^m = \left(\sum_{i=0}^C \sum_{j=0}^R (P_{ij}^m) \right) \quad (5)$$

$$Percent_Error^m = 100\% \times (Total_Errors^m / N^m) \quad (6)$$

$$Percent_Accuracy^m = 100\% - Percent_Error^m \quad (7)$$

The ground truth pixel state, I_{ij} , within each image region, superscript m , corresponds to either a high ($I = 1$) or low ($I = 0$) status. The current pixel coordinates were represented by subscript i (column) and j (row). Each classified pixel state, P_{ij} , was also either 1 or 0. An error, E , was then counted when the classified (P) and ground truth (I) pixel states at each coordinate did not align. The percentage error was calculated as the number of pixel mismatches divided by the total number of pixels in a region, and the percentage accuracy is found by subtracting that value from 100%. Errors were determined outside the fluorescent region when a pixel was in a high state, regardless of excitation state. Two different operating modes were tested in this way: a no motion test in which the camera was mounted fixedly and a high motion test during which a user translated the camera on a moving stage (Fig. 4). Each test was averaged over 5 trials.

Using the described method, motion artifacts were also quantified, since such artifacts appear as fluorescent objects in the subtraction images. Following a camera translation, the number of fluorescently labeled pixels within the phantom's previous location was divided by the total number of pixels contained in the phantom's area, as in (5). The process was repeated varying the number of loops per cycle over which binary pixel values were recorded to determine the fluorescent state ($N = 4, 6, 8$). Adjustments were made to the binary threshold, used to remove noise, to minimize the error. In addition, the average operational framerate of the system and latency were determined during this test.

Following this procedure, the motion artifacts were quantified using the pulse excitation scheme without the dense optical flow pixel tracking algorithm. A low level threshold was applied to minimize background noise, and the frame rate was set to match the equivalent frame rate determined during the point tracking tests (7.5 fps). The accuracy test results using the described point tracking method were compared to the results obtained without point tracking. Tabulated results for each test were compared for significant difference between the point tracking and non-point tracking method, using a single-tailed student's paired t -test ($n = 55$, $\alpha = 0.05$).

3. Results

3.1 Fluorescence Imaging Sensitivity

Comprehensive tests were conducted to investigate the system's sensitivity towards the imaging of fluorescent emissions, as well as to determine whether the pulsed light regime with pixel tracking provided any significant advantage over steady DC illumination. Fluorescent intensity readings for a series of dye concentrations and at each excitation intensity were experimentally obtained to determine the minimum dye concentration required for the system to achieve a range

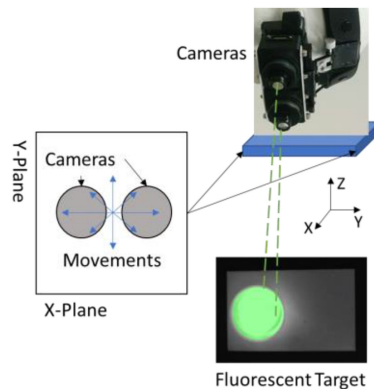


Fig. 4. Experimental configuration for camera movement test. The cameras are translated in an asterisk pattern over a fluorescent target. During camera translation, motion artifacts are counted when the target is under excitation via pulsed light, both with and without pixel tracking, and when there is no fluorescence excitation. All camera movements are in the xy-plane; the z-plane is fixed.

of SBR values. Results indicated that pulsed light imaging with pixel tracking provided significantly improved detection capabilities over the steady state at all SBR values and excitation intensities. Based on these results, the minimum concentration of PpIX that the system was able to detect in solution with an SBR of 2 was 13.2 nM using steady-state excitation and 5.9 nM using the pulsed light regime at an excitation intensity of 4 mW. Additionally, the minimum detectable dye concentration on pig skin, with high PpIX autofluorescence, at the same parameters was 227.8 nM in DC mode and 152.8 nM with pulsed light. On average, the pulsed light regime displayed an improvement factor of approximately 2.25 over the conventional DC, steady-state excitation. A graph was made of the SBR as a function of dye concentration and excitation intensity for each of the excitation methods (Fig. 5). For each dye concentration, we used dashed curves to represent the pulsed light regime with pixel tracking, and solid curves to represent steady DC mode imaging.

3.2 Fluorescent Point Tracking and Identification Accuracy

We used an imaging phantom as the ground truth to evaluate the accuracy of fluorescent pixel detection and non-fluorescent pixel rejection (Fig. 6). A small subset of pixels showed false positives in the stationary case (Fig. 6(a)), no fluorescence case (Fig. 6(b)), and under motion (Fig. 6(c)), likely due to the noise level inherent in low light imaging.

A series of experiments were performed using the accuracy-evaluating imaging phantom shown in Fig. 6, and results were analyzed with statistical rigor. Accuracy results of the fluorescence tracking regime were summarized in Table 1. Optimal results were found using a low noise threshold with a pixel value of 2, and binary pixel values were tracked and stored over $N = 6$ loops. The number of loops used to determine whether a pixel was pulsing with the excitation light source was set at 6, due to a significant improvement over 4 loops, while no significant improvement was had by increasing to 8 loops. The number of false positives and false negatives were tabulated during each test, with and without point tracking. Significance was determined on the means from each test, between the point tracking and non-tracking methods, via student's t-test ($n = 55$, $\alpha = 0.05$). Our point tracking method greatly reduced the number of motion artifacts. For example, on the imaging phantom the occurrence of motion artifacts was reduced from 98.60% to 1.54%, indicating a 45-fold reduction in motion artifacts. As a tradeoff, the false-negative rate slightly increased, likely due to the morphological operations performed on the image, which caused the loss of some image details.

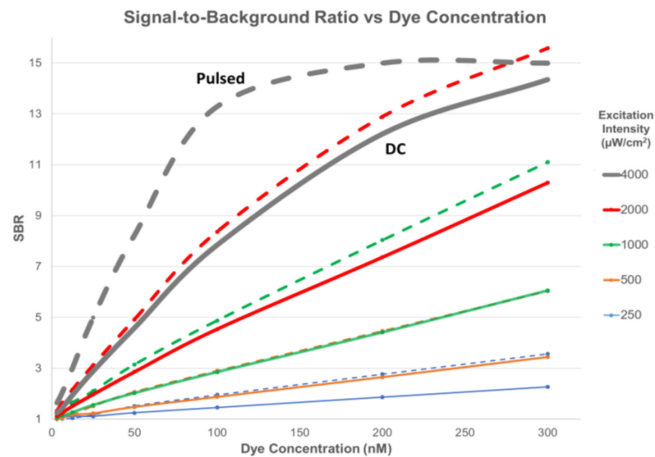


Fig. 5. Signal-to-Background Ratio (SBR) for detecting PpIX fluorescence over a range of concentrations and excitation intensities. Dye solutions were placed into separate wells of a 24-Well cell culture plate for imaging. Results show a significantly higher detected SBR when using the pulsed light with pixel tracking (dashed curve) for fluorescence excitation than when using DC mode imaging (solid curve).

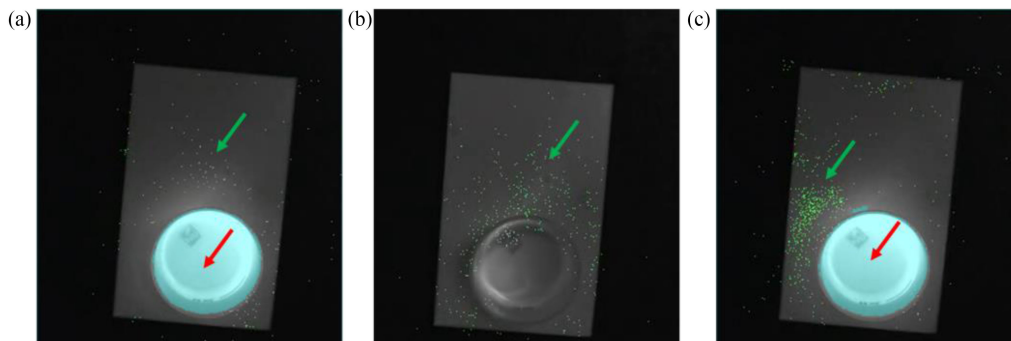


Fig. 6. Experimental setup for evaluating the accuracy of fluorescent pixel detection and non-fluorescent pixel rejection. A fluorescent dye-filled cell culture dish was placed on top of a non-fluorescent tissue phantom block. Accurate fluorescence detection based on ground truth is pseudocolored in blue, while error is in pseudocolored in green. (a) Image when the camera and target were stationary. The accurately detected fluorescence was located within the cell culture plate, indicated by the red arrow. Pixels with error were found outside the cell culture plate area, indicated by the green arrow. (b) Imaging when no fluorescence was present. The amount of error varied between frames, potentially resulting from pixel intensity fluctuation due to noise. (c) Imaging under motion. The accurately detected fluorescence was detected within the cell culture plate, indicated by the red arrow. Pixels with error were found outside the cell culture plate area, indicated by the green arrow.

3.3. Biological Imaging and Motion Artifacts Removal

In biological tissues, the system demonstrated the ability to track and capture fluorescent and reflectance images in coordination with the high and low states, respectively, of the LED excitation source (Fig. 7).

During camera and target motion, the pixel tracking and fluorescence identification removed the motion artifacts observed with pulsed light imaging (Fig. 8). This is helpful for intraoperative guidance as it removes the false positives due to motion artifacts (Supplementary Video 1 & 2). In addition to the ability to handle motion artifacts, the system offers head-mounted fluorescence imaging with augmented reality. Images captured and processed can be displayed in the wearable display in 3D with depth perception, affording users the option to move their heads in order to

TABLE 1
Results of the Fluorescence Point Tracking Accuracy Tests

		Pulsed light imaging with Pixel Tracking		Pulsed Imaging Only		P-Value
		Mean %	STD	Mean %	STD	
Motion Artifacts	Phantom	1.54	0.08	98.60	0.06	3.65E-12
	Background	3.65	0.11	99.40	0.05	6.41E-12
Positive Identification of fluorescence		99.63	0.37	99.92	0.05	9.79E-02
False Positives	Phantom	0.55	0.07	3.39	0.30	2.20E-03
	Background	0.02	0.01	0.01	0.01	5.08E-02
False Negatives		3.20	0.04	0.02	0.00	1.17E-05

Includes mean and standard deviation of the percentage of false positives in the image background and on the tissue phantom (without motion), the percent of false negatives in the target fluorescence, and the amount of motion artifacts as a percentage of the area of the object that has moved between sequential frames. Results were analyzed for significant differences between the point tracking and non-tracking pulsed light methods.

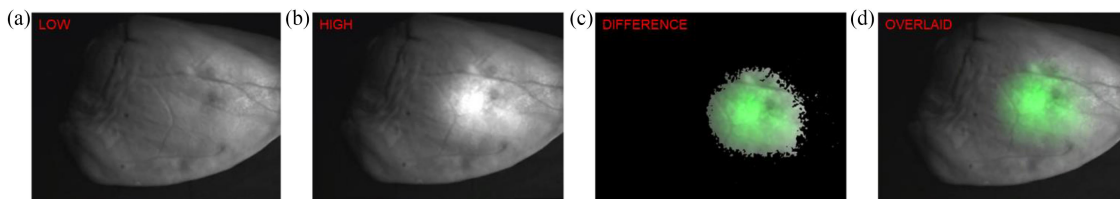


Fig. 7. Pig ear with topically applied PpIX solution (green), imaged under pulsed excitation. (a) Low pulse state without fluorescence excitation, reflectance alone is imaged under ambient lighting only. (b) High pulse state with excitation, in which both fluorescence and reflectance are imaged. (c) The subtraction result from the sequential High and Low state frames: the resulting difference image represents fluorescence without reflectance, pseudocolored in green. (d) The composite image of the difference image with reflectance image. Fluorescence is pseudocolored in green.

improve or alter their line of sight while also negating the need of fixing their pose to stabilize the camera.

Furthermore, tests were conducted to count missed states to quantify the efficiency of pulsation coordination and interleaved acquisition throughout the system. The percentage of missed frames was 1.22% and 3.88%, during low and high motion tests, respectively. A slightly greater number of missed states were counted with higher motion, as expected. The low percentage of missed states is very promising for system deployment in a realistic surgical setting, and using a mini-PC without a dedicated GPU.

4. Discussion

This study demonstrated a novel method of combining computer vision techniques and imaging hardware design to solve clinically relevant problems. The system effectively reduced motion artifacts from 98.60% to 1.54%, compared to conventional pulsed light imaging. This represents a 64-fold reduction of motion artifacts. In realistic surgical situations motion is always present, whether a head-mounted, handheld, or cart-mounted imaging system is used. The near-total motion artifact reduction represents an important step towards broadly applying pulsed fluorescence imaging in the operating room as a clinical tool.

We have evaluated the accuracy of fluorescence tracking in a realistic environment by selecting PpIX as the model fluorescence system, as porphyrins are endogenous fluorophores widely present in biological tissues and establish a high autofluorescence background. In our opinion, the highly autofluorescent environment provides a better model system for simulating surgical

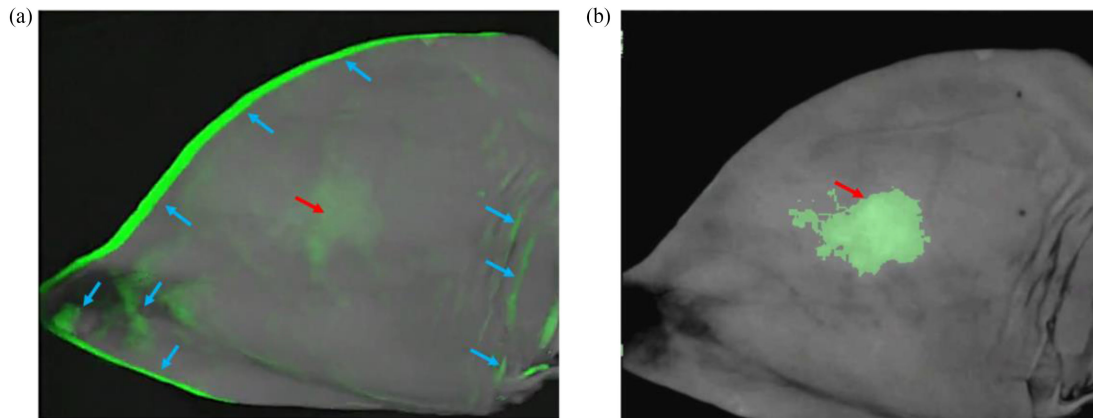


Fig. 8. The system removes motion artifacts in pulsed light imaging. (a) Image of a pig ear captured using conventional pulsed light imaging following a camera translation. Blue arrows indicate the motion artifacts incurred by subtracting sequential frames acquired during the movement. The disparity in ear location between sequential frames due to camera movement caused the motion artifact. (b) The same pig ear was captured with pixel tracking and fluorescence pixel identification. Minimal motion artifacts were observed. The red arrow indicates fluorescence.

settings. In this study, the noise was also reduced by increasing the number of loops per cycle over which pixel intensities were tracked. Using too many loops resulted in lower frame rates and lower positive identification rates. During these experiments, it was found that random pixel variations, noise, or object motion could cause a pixel's recorded values to vary from the ground truth. When implementing a greater number of loops, it was therefore beneficial to allow for an error margin in the tracked pixel values. For example, when tracking a pixel's binary sequence over 8 loops, the ground truth of high and low excitation states may be 01010101, where 0's correspond to the low states, and 1's are the high states. However, allowing a tracked pixel with one binary value error, such as 01010001, to be accepted as fluorescence may improve positive detection rates. We have found that allowing for an error is more likely to prove beneficial with an increased number of tracked loops ($N > 6$).

This study demonstrated enhanced SBR for the detected fluorescence emissions over a range of dye concentrations. In our option, the improved SBR with a near-total motion artifact reduction represents an important step to further the application of pulsed light imaging to clinical translation. The SBR enhancements were due to the separation of the fluorescence signal from the bright reflectance background with accurate localization. Our findings align with previous findings of other studies of pulsed fluorescence imaging [25]–[30]. It should be noted that imaging under darkroom conditions, or at least very low background conditions, will further improve SBR while also reducing the motion artifact effect by reducing the intensity of the subtracted difference images. However, in this study, we did not use the ideal darkroom lab condition for quantifying SBR or motion artifacts as such conditions are not readily achieved in various practical settings (e.g., OR, clinic, in-transit/expeditionary medicine). In our opinion, applying pulsed light with pixel tracking can help improve fluorescence imaging under any lighting conditions; however, the effect may be most useful under non-ideal settings with a high ambient light background similar to an OR setting.

As expected, the presence of missed or mismatched states due to imperfect timing (e.g., the camera identifies a captured frame as high when it has actually captured a low state, or vice versa) likely corresponds to the different clock signals of cameras, the microcontroller, the PC, and serial communication protocols. Also, low USB or other data transmission bandwidth from the imaging sensors could result in delays and desynchronization. This can be remedied by synchronizing the clock for these components and applying serial communication interfaces with higher bandwidth. With the current method, the framerate was effectively halved due to the

combination of fluorescence and non-fluorescence states using the pulsed light regime. To deploy this method in the future in a clinical system, high-framerate image sensors will be ideal, such as high-speed CMOS sensors with frame rates over 120 fps (e.g., effective framerate will be 60 fps). Fortunately, there are a wide selection of high-speed, high-resolution CMOS imaging sensors with desirable quantum efficiency. In our study, we implemented GPU parallelization. In the literature, parallel processing has also improved system performance when an increased processing load has proven detrimental to efficiency and speed. Future work could incorporate the latest graphic card and more extensive kernel coding for improved GPU data handling.

5. Conclusion

In summary, we demonstrated a 45-fold reduction of motion artifacts by combining pixel tracking and fluorescence pixel identification with pulsed light imaging. Furthermore, fluorescence imaging SBR is also improved. On average, the SBR of detected fluorophores using pulsed light was over 2 times larger than that found using conventional DC fluorescence excitation. Our results indicate that pixel tracking and temporal gating can improve fluorescence imaging, especially for realistic clinical settings where there is a high ambient light background.

Acknowledgment

The U.S. Government is authorized to reproduce and distribute reprints for Governmental purposes notwithstanding any copyright notation thereon. The views and conclusions contained herein are those of the authors and should not be interpreted as necessarily representing the official policies or endorsements, either expressed or implied, of the U.S. Air Force or the U.S. Government.

References

- [1] M. Koch and V. Ntziachristos, "Advancing surgical vision with fluorescence imaging," *Annu. Rev. Med.*, vol. 67, pp. 153–164, 2016.
- [2] M. J. Landau, D. J. Gould, and K. M. Patel, "Advances in fluorescent-image guided surgery," *Ann. Transl. Med.*, vol. 2, no. 20, 2016, Art. no. 392.
- [3] T. Nagaya, Y. A. Nakamura, P. L. Choyke, and H. Kobayashi, "Fluorescence-Guided surgery," *Front. Oncol.*, vol. 7, 2017, Art. no. 314.
- [4] C. A. Mela, C. Patterson, W. K. Thompson, F. Papay, and Y. Liu, "Stereoscopic integrated imaging goggles for multimodal intraoperative image guidance," *PLoS One*, vol. 10, no. 11, 2015, Art. no. e0141956.
- [5] W. F. Chen, H. Zhao, T. Yamamoto, H. Hara, and J. Ding, "Indocyanine green lymphographic evidence of surgical efficacy following microsurgical and supermicrosurgical lymphedema reconstructions," *J. Reconstr. Microsurg.*, vol. 32, no. 9, pp. 688–698, Nov. 2016.
- [6] C. A. Mela, F. A. Papay, and Y. Liu, "Intraoperative fluorescence imaging and multimodal surgical navigation using goggle system," *Methods Mol. Biol.*, vol. 1444, pp. 85–95, 2016.
- [7] C. Mela and Y. Liu, "Comprehensive characterization method for a fluorescence imaging system," *Appl. Opt.*, vol. 58, no. 30, pp. 8237–8246, Oct. 20, 2019.
- [8] C. A. Mela, D. P. Lemmer, F. S. Bao, F. Papay, T. Hicks, and Y. Liu, "Real-time dual-modal vein imaging system," *Int. J. Comput. Assist. Radiol. Surg.*, vol. 14, no. 2, pp. 203–213, Feb. 2019.
- [9] S. A. Valente, Z. Al-Hilli, D. M. Radford, C. Yanda, C. Tu, and S. R. Grobmyer, "Near infrared fluorescent lymph node mapping with indocyanine green in breast cancer patients: A prospective trial," *J. Amer. Coll. Surg.*, vol. 228, no. 4, pp. 672–678, Apr. 2019.
- [10] S. B. Mondal, C. M. O'Brien, K. Bishop, R. C. Fields, J. A. Margenthaler, and S. Achilefu, "Repurposing molecular imaging and sensing for cancer image-guided surgery," *J. Nucl. Med.*, vol. 61, no. 8, pp. 1113–1122, Aug. 2020.
- [11] D. Shen *et al.*, "Selective imaging of solid tumours via the calcium-dependent high-affinity binding of a cyclic octapeptide to phosphorylated annexin A2," *Nat. Biomed. Eng.*, vol. 4, no. 3, pp. 298–313, Mar. 2020.
- [12] T. T. Quang, W. F. Chen, F. A. Papay, and Y. Liu, "Dynamic, real-time, fiducial-free surgical navigation with integrated multimodal optical imaging," *IEEE Photon. J.*, vol. 13, no. 1, Feb. 2021, Art. no. 3900113.
- [13] E. Belykh *et al.*, "Intraoperative fluorescence imaging for personalized brain tumor resection: Current state and future directions," *Front. Surg.*, vol. 3, 2016, Art. no. 55.
- [14] H. Stepp and W. Stummer, "5-ALA in the Management of malignant glioma," *Lasers Surg. Med.*, vol. 50, no. 5, pp. 399–419, 2018.

- [15] O. Kulyk, S. H. Ibbotson, H. Moseley, R. M. Valentine, and I. D. Samuel, "Development of a handheld fluorescence imaging device to investigate the characteristics of protoporphyrin IX fluorescence in healthy and diseased skin," *Photodiagnosis Photodyn. Ther.*, vol. 12, no. 4, pp. 630–639, 2015.
- [16] S. Gao, S. B. Mondal, N. Zhu, R. Liang, S. Achilefu, and V. Grueva, "Image overlay solution based on threshold detection for a compact near infrared fluorescence goggle system," *J. Biomed. Opt.*, vol. 20, no. 1, 2015, Art. no. 016018.
- [17] J. M. Warram *et al.*, "A radiometric threshold for determining presence of cancer during fluorescence-guided surgery," *J. Surg. Oncol.*, vol. 112, no. 1, pp. 2–8, 2015.
- [18] Y. Liu *et al.*, "Near-infrared fluorescence goggle system with complementary metal-oxide-semiconductor imaging sensor and see-through display," *J. Biomed. Opt.*, vol. 18, no. 10, 2013, Art. no. 101303.
- [19] Y. Liu *et al.*, "First in-human intraoperative imaging of HCC using the fluorescence goggle system and transarterial delivery of near-infrared fluorescent imaging agent: A pilot study," *Translational Res.*, vol. 162, no. 5, pp. 324–331, 2013.
- [20] K. He *et al.*, "Comparison between the indocyanine green fluorescence and blue dye methods for sentinel lymph node biopsy using novel fluorescence image-guided resection equipment in different types of hospitals," *Translational Res.*, vol. 178, pp. 74–80, 2016.
- [21] S. B. Mondal *et al.*, "Binocular goggle augmented imaging and navigation system provides real-time fluorescence image guidance for tumor resection and sentinel lymph node mapping," *Sci. Rep.*, vol. 5, 2015, Art. no. 12117.
- [22] C. A. Mela, C. Patterson, W. K. Thompson, F. Papay, and Y. Liu, "Stereoscopic integrated imaging goggles for multimodal intraoperative image guidance," *PLoS One*, vol. 10, no. 11, 2015, Art. no. e0141956.
- [23] P. Shao *et al.*, "Designing a wearable navigation system for image-guided cancer resection surgery," *Ann. Biomed. Eng.*, vol. 42, no. 11, pp. 2228–2237, 2014.
- [24] C. A. Mela, C. L. Patterson, and Y. Liu, "A miniature wearable optical imaging system for guiding surgeries," in *SPIE Photonics West*, San Francisco, CA, USA, B. W. Pogue and S. Gioux, Eds., Feb. 7–12, 2015, vol. 9311: SPIE.
- [25] D. Piccolo and D. Kostaki, "Photodynamic therapy activated by intense pulsed light in the treatment of nonmelanoma skin cancer," *Biomedicine*, vol. 6, no. 1, 2018, Art. no. 18.
- [26] C. Boudreau, T.-L. Wee, Y.-R. Duh, M. P. Couto, K. H. Ardakani, and C. M. Brown, "Excitation light dose engineering to reduce Photo-bleaching and Photo-toxicity," *Sci. Rep.*, vol. 6, 2016, Art. no. 30892.
- [27] K. Sexton *et al.*, "Pulsed-light imaging for fluorescence guided surgery under normal room lighting," *Opt. Lett.*, vol. 38, no. 17, pp. 3249–3252, 2013.
- [28] K. J. Sexton, Y. Zhao, S. C. Davis, S. Jiang, and B. W. Pogue, "Optimization of fluorescent imaging in the operating room through pulsed acquisition and gating to ambient background cycling," *Biomed. Opt. Exp.*, vol. 8, no. 5, pp. 2635–2648, 2017.
- [29] Z. Chen, N. Zhu, S. Pacheco, X. Wang, and R. Liang, "Single camera imaging system for color and near-infrared fluorescence image guided surgery," *Biomed. Opt. Exp.*, vol. 5, no. 8, pp. 2791–2797, 2014.
- [30] B. Zhu, J. C. Rasmussen, and E. M. Sevick-Muraca, "Non-invasive fluorescence imaging under ambient light conditions using a modulated ICCD and laser diode," *Biomed. Opt. Exp.*, vol. 5, no. 2, pp. 562–572, 2014.
- [31] A. Behrooz *et al.*, "Multispectral open-air intraoperative fluorescence imaging," *Opt. Lett.*, vol. 42, no. 15, pp. 2964–2967, 2017.
- [32] N. S. van den Berg *et al.*, "(Near-Infrared) fluorescence-guided surgery under ambient light conditions: A next step to embedment of the technology in clinical routine," *Ann. Surg. Oncol.*, vol. 23, no. 8, pp. 2586–2595, 2016.
- [33] B. D. Lucas and T. Kanade, "An iterative image registration technique with an application to stereo vision," in *Proc. Imag. Understanding Workshop*, Vancouver, BC, CAN, 1981, vol. 2, pp. 674–679.
- [34] OpenCV. "Optical flow," Accessed: January 8, 2018. [Online]. Available: https://docs.opencv.org/3.4/d7/d8b/tutorial_py_lucas_kanade.html
- [35] G. Farneback, "Two-Frame motion estimation based on polynomial expansion," in *Scand. Conf. Image Anal.*, SWE Halmstad, J. Bigun, and T. Gustavsson, Eds., Jun. 29 - Jul. 2, 2003, vol. 2749, Berlin Heidelberg, Germany: Springer, in Lecture Notes in Computer Science.
- [36] G. Wagnieres *et al.*, "An optical phantom with Tissue-like properties in the visible for use in PDT and fluorescence spectroscopy," *Phys. Med. Biol.*, vol. 42, pp. 1415–1426, 1997.